

Giant anisotropic magnetoresistance through a tilted molecular π -orbital

Dongzhe Li,^{1,2,*} Fabian Pauly,^{3,1} and Alexander Smogunov⁴

¹*Department of Physics, University of Konstanz, 78457 Konstanz, Germany*

²*Department of Physics, Technical University of Denmark, DK-2800 Kongens Lyngby, Denmark*

³*Okinawa Institute of Science and Technology Graduate University, Onna-son, Okinawa 904-0495, Japan*

⁴*SPEC, CEA, CNRS, Université Paris-Saclay, CEA Saclay 91191 Gif-sur-Yvette Cedex, France*

(Dated: March 6, 2021)

Anisotropic magnetoresistance (AMR), originating from spin-orbit coupling (SOC), is the sensitivity of the electrical resistance in magnetic systems to the direction of spin magnetization. Although this phenomenon has been experimentally reported for several nanoscale junctions, a clear understanding of the physical mechanism behind it is still elusive. Here we discuss a novel concept based on orbital symmetry considerations to attain a significant AMR of up to 95% for a broad class of π -type molecular spin-valves. It is illustrated at the benzene-dithiolate molecule connected between two monoatomic nickel electrodes. We find that SOC opens, via spin-flip events at the ferromagnet-molecule interface, a new conduction channel, which is fully blocked by symmetry without SOC. Importantly, the interplay between main and new transport channels turns out to depend strongly on the magnetization direction in the nickel electrodes due to the tilting of molecular orbital. Moreover, due to multi-band quantum interference, appearing at the band edge of nickel electrodes, a transmission drop is observed just above the Fermi energy. Altogether, these effects lead to a significant AMR around the Fermi level, which even changes a sign. Our theoretical understanding, corroborated in terms of *ab initio* calculations and simplified analytical models, reveals the general principles for an efficient realization of AMR in molecule-based spintronic devices.

PACS numbers:

Spin-orbit coupling (SOC) is the quantum effect of relativistic nature, which links electronic spin and orbital degrees of freedom. It is at the origin of a wide range of intriguing phenomena in condensed matter physics such as the Rashba effect, magneto-crystalline anisotropy, AMR, etc. Although AMR is the oldest known magneto-transport effect, it is of high timeliness due to the recent development of precise experimental tools to study magnetic systems at the atomic scale. For instance, the tunneling AMR (TAMR) was first observed by Bode *et al.*¹ in scanning tunneling spectroscopy (STM), which was also reported in Ref. 2–4. In addition, a very large TAMR was reported in various magnetic tunnel junctions^{5–8}. In the contact regime, an enhanced ballistic AMR in atomic contacts was predicted theoretically^{9–13} and observed experimentally via mechanically controllable break junctions (MCBJ)^{14–16} or STM¹⁷. Besides, an electrically tunable AMR was found in the Coulomb blockade regime in a ferromagnetic semiconductor single-electron transistor¹⁸. Recently, several experimental works^{4,19–23} on tuning AMR in single-molecule junctions have stimulated a new research venue in molecular spintronics, which is the so-called molecular anisotropic magnetoresistance (AMR)²⁴. Quantitatively, AMR is defined as $AMR = (G_{\parallel} - G_{\perp})/G_{\perp}$, where G_{\parallel} and G_{\perp} are electrical conductances for parallel and perpendicular orientations of the magnetization, respectively, with regard to the current flow.

In bulk ferromagnetic metals, the AMR is less than 5%²⁵ due to quenched orbital moments. Its value can increase dramatically in low-dimensional nanostructures such as monoatomic wires due to enhanced orbital moments and the high sensitivity of the local electronic structure to the magnetization direction induced by the SOC^{10,13,26}. Unlike metallic atomic contacts, in molecular junctions the transport between two electrodes is typically mediated by a relatively

weakly bound molecule. Therefore, molecular orbitals are expected to preserve their symmetry and localized nature. In the collinear magnetic case without SOC, it has been shown that non-magnetic organic molecule can act as a “half-metallic” conductor due to either orbital symmetry arguments^{27,28} or quantum interference effects^{29,30}, leading to nearly fully spin-polarized conduction. In addition, a nearly perfect spin filtering was also reported when the vanadium-benzene wire is placed between two magnetic electrodes³¹. In the non-collinear magnetic case with SOC, both the band structures of the ferromagnetic electrodes and the selective hybridization between electrode and molecular states can be largely modified, yielding a large AMR.

Here, using fully relativistic density functional theory (DFT) calculations combined with a scattering theory, we demonstrate how a giant AMR of around 95% at the Fermi level (E_F) can be obtained by designing a molecular junction, in which molecular orbitals selectively hybridize with d bands of ferromagnetic electrodes. We discuss the mechanism using a simple model system, consisting of a benzene-dithiolate (BDT) molecule joining two semi-infinite monoatomic Ni chains. The conductance is fully spin-polarized without SOC since the spin-up channel is blocked at the ferromagnet-molecule interface by orbital symmetry mismatch between molecular and electrode states. If SOC is switched on, a new spin-up-derived channel fully opens due to spin-flip events. Furthermore, the SOC distinguishes the transmissions for different magnetic orientations when the π -shaped molecular orbitals couple to the Ni d bands, giving rise to a very high and energy-dependent AMR in the vicinity of E_F . We rationalize the DFT results by a simple tight-binding model. Our findings provide guidelines of how an optimal AMR can be achieved in π -conjugated molecular junctions

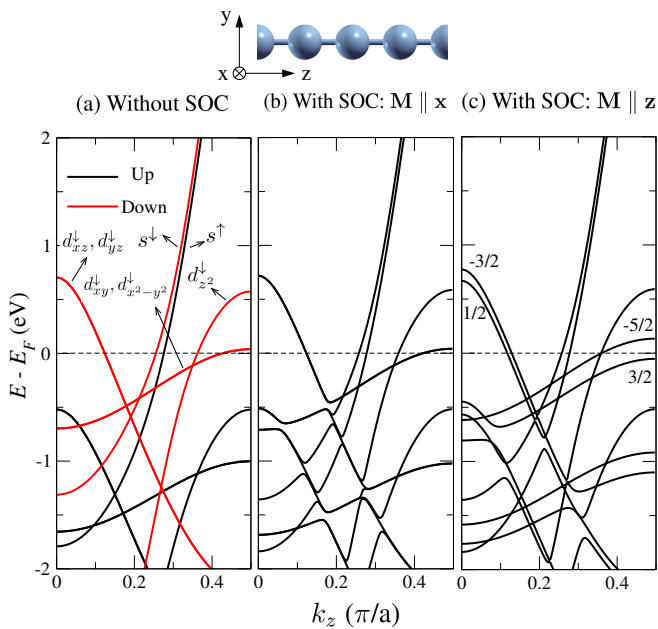


FIG. 1: Band structure of a Ni monoatomic wire at the equilibrium lattice spacing of $a = 2.10 \text{ \AA}$ without SOC (a) and with SOC for spin magnetization along the x (b) or the z (c) axis. The spin-up and -down bands in (a) are visualized by black and red lines, respectively. The bands are labeled by their orbital moment (a) or by total angular momentum (c) along the wire axis z .

based on clear symmetry arguments.

The DFT calculations in the local density approximation (LDA) have been performed using the plane-wave QUANTUM ESPRESSO (QE) package³². The coherent electron transport was evaluated by PWCOND³³ based on the scattering formalism with ultra-soft pseudopotentials, which is a part of the QE package. The SOC, crucial for AMR, is taken into account via fully relativistic pseudopotentials³⁴. The elastic conductance is evaluated from the total electron transmission at the Fermi energy using the Landauer-Büttiker formula, $G = G_0 T(E_F)$, where $G_0 = e^2/h$ is the conductance quantum per spin. For collinear magnetic systems without SOC effects the total transmission is the sum of two independent spin transmissions, $T(E_F) = T_\uparrow(E_F) + T_\downarrow(E_F)$. Structural optimizations of molecular junctions have been performed without SOC using face-centered cubic Ni(111) crystalline electrodes. For transport calculations they were replaced with semi-infinite Ni chains. More details regarding computational details can be found in the supplementary material.

The objective of this work is to demonstrate theoretically the mechanism to obtain giant molecular AMR effects based on orbital symmetry arguments. Here, we focus on the influence of SOC on quantum transport across a BDT molecule sandwiched between two semi-infinite Ni leads, as sketched in Fig. 2(a). Note that for better comparison to experiment electrodes with a larger cross section should be used, but we expect that our simplified model captures the relevant mechanisms, allowing at the same time a detailed analysis at reduced computational cost.

We start by studying the band structure of a Ni atomic chain, since it provides information on the number of conduction channels in the electrodes. Let us first discuss the band structure of the Ni chain without SOC, as plotted in Fig. 1(a). For spin-up (majority spin), only one largely dispersive s band crosses E_F in the middle of the one-dimensional Brillouin zone, while six d channels are available for spin-down (minority spin). We mark explicitly two twofold degenerate bands, namely $d_{xz}^\downarrow; d_{yz}^\downarrow$ with a wide negative dispersion and $d_{x^2-y^2}^\downarrow; d_{xy}^\downarrow$ with a narrow positive dispersion, which will be important in the following. When the SOC is included, the band structures for magnetization M chosen parallel to the x axis ($M \parallel x$) and $M \parallel z$ are very different, as visible in Fig. 1(b) and 1(c). For $M \parallel x$ the band splitting by SOC is tiny, so band dispersions are very similar to those without SOC. Interestingly, a pseudo-gap opens at about -0.45 eV , finally causing a large AMR of more than 160% for the perfect Ni chain in that energy region. For $M \parallel z$ the SOC lifts the degeneracy of both $d_{xz}^\downarrow; d_{yz}^\downarrow$ and $d_{x^2-y^2}^\downarrow; d_{xy}^\downarrow$ bands, resulting in sets of $m_j = -3=2; 1=2$ and $m_j = -5=2; 3=2$ bands with similar dispersion, respectively, where m_j is the projection of the total angular momentum along the z axis. The findings are in excellent agreement with previous theoretical calculations^{9,24}.

Now we discuss the transport properties of the Ni-BDT-Ni molecular junction, shown in Fig. 2. After geometry optimization with Ni(111) crystalline electrodes, we find that the BDT molecule prefers to slightly rotate in the yz plane, which is consistent with previous theoretical results³⁵⁻³⁷. The highest occupied molecular orbital (HOMO) of the BDT molecule is of odd symmetry with respect to the yz plane, originating mainly from p_x atomic orbitals of carbon and sulfur atoms. This is visible in Fig. 2(a), where the HOMO is presented together with the projected density of states (PDOS) of BDT in the molecular junction configuration. By symmetry, HOMO can only couple to d_{xz}^\downarrow and d_{xy}^\downarrow but not to s states of the Ni chains. The PDOS therefore shows a very sharp HOMO peak for spin up around E_F but a much broader feature for spin down due to larger hybridization. This is further reflected, see Fig. 2(b), in a complete blocking of the spin-up transmission around E_F , where only the Ni s channel is present, while a finite spin-down transmission is provided by the Ni d_{xz}^\downarrow channel, which generates a fully spin-polarized conductance due to symmetry arguments proposed by us recently²⁷. Interestingly, a pronounced dip in the spin-down transmission is observed very close to the Fermi energy. It appears right above the Ni d_{xy}^\downarrow band (see Fig. 1(a)) and results from destructive interference, as will be discussed later.

We now turn our attention to SOC effects on electron transport for different spin magnetization configurations, namely $M \parallel x$ and $M \parallel z$, as shown in Fig. 2(c). We focus on the energy range close to the Fermi energy. Clearly, the transmission functions for the two magnetic orientations are very different. In particular, the transmission for $M \parallel x$ increases up to about 2 at about 20 meV below E_F , with $G_0 = e^2/h$. This sharp peak originates from the HOMO spin-up molecular orbital, which was inactive by symmetry before, but couples

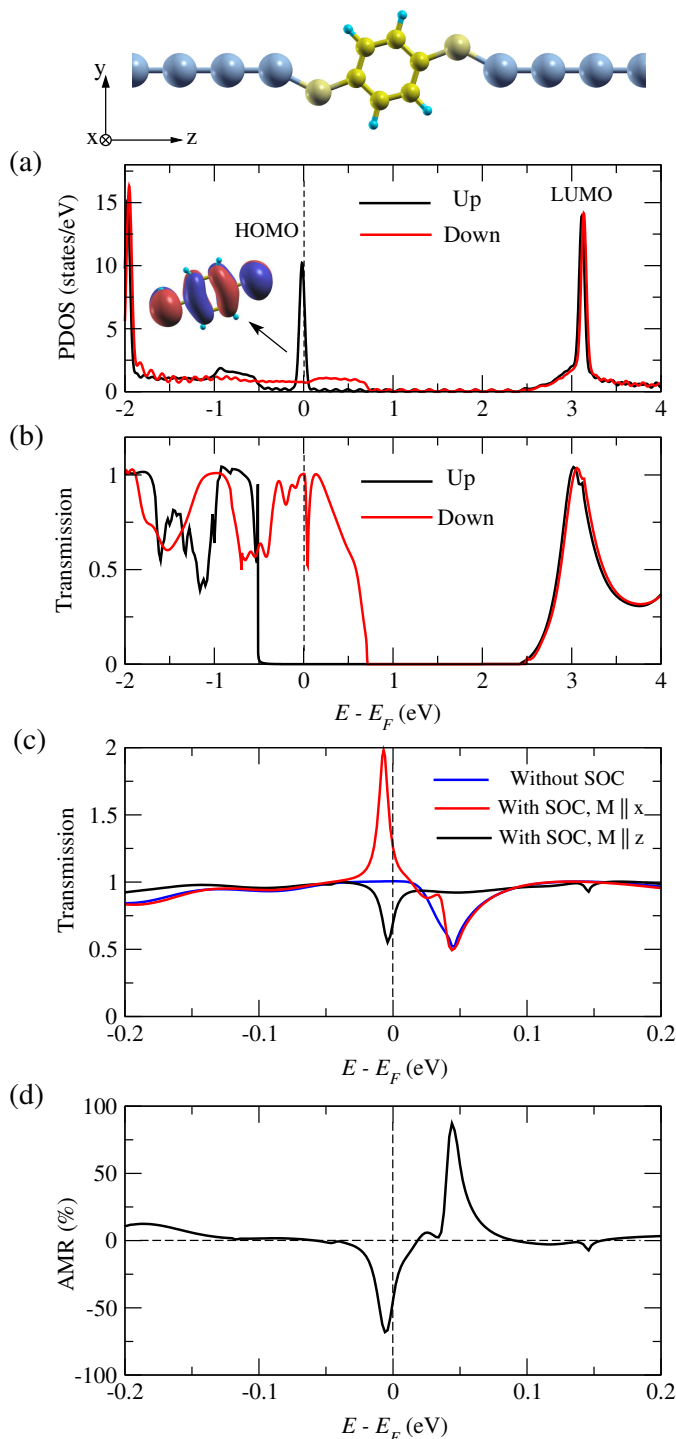


FIG. 2: Ni wire/BDT junction: (a) Spin-resolved PDOS on the BDT molecule without SOC. Wave function of the HOMO orbital of the free molecule is shown in inset. (b) Spin-resolved transmission function without SOC. A dip is observed for spin down right above the Fermi level. (c) Total transmissions of the junction without SOC (blue) and with SOC for $M \parallel x$ (red) and $M \parallel z$ (black) configurations. (d) Energy-dependent AMR defined as $AMR(E) = (T_z(E) - T_x(E))/T_x(E)$. A giant AMR with a changing sign is found around E_F .

with electrode states through the SOC term. For the $M \parallel z$ configuration, on the contrary, a dip rather than a peak is observed in the transmission at this energy, which results in an AMR as large as -74% , see Fig. 2(d).

To explore the origin of this huge AMR, we plot in Fig. 3 the transmission eigenvalues for both magnetic orientations. Two eigenchannels are found for both cases instead of one spin-down eigenchannel without SOC. The results for the $M \parallel x$ configuration indicate that the two channels are independent. The x component of the magnetic moment (M_x , averaged in xy plane) of each channel at $E - E_F = -20$ meV, shown as insets, confirm that the highly transmissive channel (red) is related to the HOMO spin-down orbital due to a slightly negative spin moment on the molecule, while the other one (black) stems from the HOMO spin-up orbital, as indicated by the very large and positive spin moment on the BDT. A similar conclusion is reached by comparing the eigenchannel transmissions for $M \parallel x$ to the spin-resolved transmission in Fig. 2(b). Note that both channels describe the propagation of electrons between spin-down Ni states: The first one (red) conserves the electron spin while the second one (black) involves spin-flip processes at the metal-molecule interfaces activated by the SOC term in the Hamiltonian. For $M \parallel z$, on the contrary, the two channels mix, exhibiting in particular a crossing at $E - E_F = -20$ meV and a lower total transmission at that E compared to the $M \parallel x$ case, see Fig. 2(c).

Interestingly, the transmission for the $M \parallel x$ configuration shows a dip at about 40 meV above the Fermi energy (see Fig. 2(c)). It is again related to the edge of the Ni $d_{x^2-y^2}^{\downarrow}; d_{xy}^{\downarrow}$ bands, which is not modified by the SOC in this situation. On the contrary, for $M \parallel z$ this band is largely split into $m_j = 3=2$ and $m_j = -5=2$ subbands (see Fig. 1(c)). Consequently, the transmission dip moves with the $m_j = -5=2$ band to higher energies and appears much less pronounced at around 150 meV. In summary, a very large AMR of a variable sign is found in the energy window between -20 and 60 meV as demonstrated in Fig. 2(d). Note that a large AMR of around 30% has previously been measured for Ni-BDT-Ni molecular junctions by Yamada *et al.*¹⁹ and may be explained by our results.

Note that a range of similar metal-benzene complexes, including a model Ni/benzene junction, has been reported by Otte *et al.*²⁴. The benzene molecule (without linking group of sulfur) was however oriented perpendicular to the transport direction (in the xy plane) which is different to our geometry (Fig. 2(a)). Very large AMR of about a few hundred were reported at $E - E_F = -450$ meV, attributed to the SOC-induced pseudo-gap in the Ni wire for $M \parallel x$ and to the orbital-symmetry filtering of the molecule at that specific energy (turning the pseudo-gap into the true transport gap). However, almost no AMR was found around the Fermi energy. Giant AMR ratios, found in our Ni/BDT junctions close to the Fermi level, are generated, on the contrary, by SOC and interference effects at the molecule/Ni wire interfaces and do not rely on fine details of the Ni wire band structure. In particular, spin-flip processes at the Ni/molecule contacts open a new conduction channel (fully closed by symme-

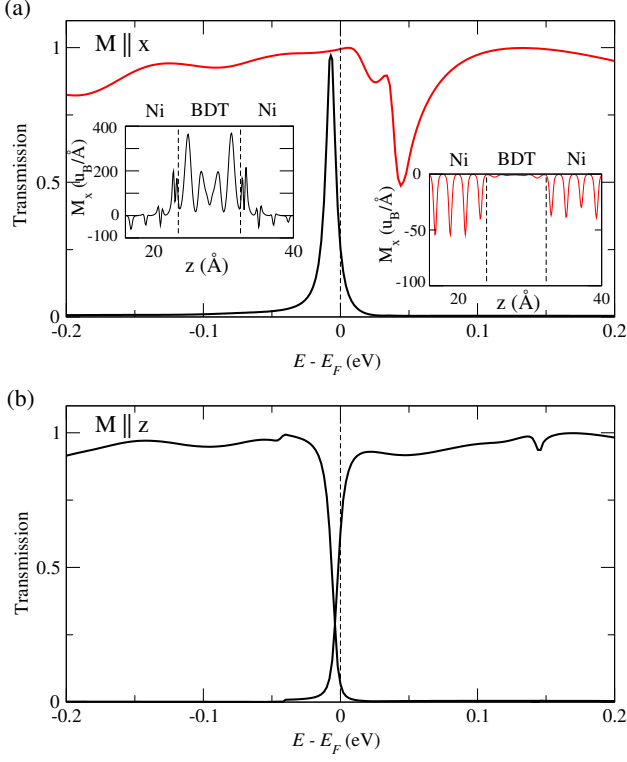


FIG. 3: (a) Transmission eigenvalues for the $M \parallel x$ magnetic configuration, showing two independent channels (red and blue lines). Insets: magnetic moments (x-components), averaged in the xy plane, as a function of z for both eigenchannels at $E - E_F = -20$ meV. Spin-flip (black) or spin-conserving (red) propagation of an electron is clearly seen for the HOMO-up or -down related channels, respectively. (b) Transmission eigenvalues for the $M \parallel z$ magnetic configuration, showing the mixing of two channels.

try in the absence of SOC), the interplay of which with another channels depends strongly on the magnetization direction. We argue, therefore, that the physical mechanism behind giant AMR in our case is not the same as in Ref. [24]. Besides, we also reproduce extremely large AMR of more than 8000% at $E - E_F = -450$ meV (see Fig. S1 in the supplementary material).

Let us note that DFT contains uncertainties with regard to the energetic ordering of molecular levels and their alignment with the electrode states, while we expect the metallic Ni states to be well described. For improvements computationally demanding quasiparticle methods, such as the GW approach, would need to be coupled to our quantum transport calculations³⁸. It may be argued that the quasiparticle corrections will mostly affect the unoccupied orbitals by opening the HOMO-LUMO gap, while the energy position of the HOMO is only slightly altered. Since we find that the spin transport through the Ni-BDT-Ni system is dominated by the HOMO, we hope that our DFT results and predictions are reliable.

In order to explain our results for the AMR, we study the SOC term of the Hamiltonian, which can be written as $H_{\text{SOC}} = \mathbf{L} \cdot \mathbf{S}$, where ξ is the effective SOC constant and \mathbf{L}

and $\mathbf{S} = \boldsymbol{\sigma} = 2$ are the orbital momentum and spin operators of an electron, respectively. In the following we will always fix the angular momentum axis to the z direction, while we will choose the spin-quantization axis along x or z for $M \parallel x$ or $M \parallel z$ magnetic configurations, respectively. For $M \parallel x$ the effective spin-orbit Hamiltonian can thus be written as a 2×2 matrix in spin space,

$$H_{\text{SOC}}^x = \frac{\xi}{4} \begin{bmatrix} L_+ + L_- & -i(L_+ - L_-) - 2iL_z \\ -i(L_+ - L_-) + 2iL_z & -L_+ - L_- \end{bmatrix}; \quad (1)$$

where $L_{\pm} = L_x \pm iL_y$. For $M \parallel z$ the same SOC Hamiltonian has the form

$$H_{\text{SOC}}^z = \frac{\xi}{2} \begin{bmatrix} L_z & L_- \\ L_+ & -L_z \end{bmatrix}; \quad (2)$$

As discussed before, by symmetry the molecular HOMO can only hybridize with d_{xz} and d_{xy} Ni orbitals. Therefore, on Ni apex atoms, where the SOC is essential, it can be expressed as

$$\begin{aligned} |\Psi_{\text{HOMO}}^\alpha\rangle &= A_\alpha |d_{xz}\rangle + B_\alpha |d_{xy}\rangle \\ &= A_\alpha (|-1\rangle - |1\rangle) + B_\alpha (|-2\rangle - |2\rangle) \end{aligned} \quad (3)$$

with \uparrow, \downarrow and some spin-dependent coefficients A_α and B_α . Here, the real harmonics d_{xz} and d_{xy} (not necessarily normalized) are expanded in terms of complex ones with orbital moment $m = \pm 1$ and $m = \pm 2$.

In the absence of SOC the HOMO spin-up orbital is decoupled from the Ni electrodes, where only the s-band is available around the Fermi energy. We apply now the SOC Hamiltonian to the HOMO spin-up orbital at the Ni apex atoms. For the $M \parallel x$ orientation we get

$$H_{\text{SOC}}^x |\Psi_{\text{HOMO}}^\uparrow\rangle = \frac{\xi}{2} \begin{bmatrix} B_\uparrow |d_{xz}\rangle + A_\uparrow |d_{xy}\rangle \\ -\sqrt{6}iA_\uparrow |0\rangle - i(B_\uparrow + A_\uparrow) |d_{yz}\rangle + i(A_\uparrow - 2B_\uparrow) |d_{x^2-y^2}\rangle \end{bmatrix}; \quad (4)$$

We notice that a nonzero spin-down component will couple the HOMO spin-up orbital to spin-down Ni bands of mainly $d_{yz}^\downarrow; d_{x^2-y^2}^\downarrow$ character available at E_F . So a new conduction channel will be opened through spin-flip processes. On the other hand, the HOMO spin-down orbital will mainly conduct through the other spin-down Ni bands of $d_{xz}^\downarrow; d_{xy}^\downarrow$ character. Moreover, it is clear that $\langle \Psi_{\text{HOMO}}^\downarrow | H_{\text{SOC}}^x | \Psi_{\text{HOMO}}^\uparrow \rangle = 0$, so that HOMO spin-up and spin-down orbitals remain strictly orthogonal, rendering the two conduction channels independent. For the $M \parallel z$ orientation an analogous reasoning leads to

$$H_{\text{SOC}}^z |\Psi_{\text{HOMO}}^\uparrow\rangle = \frac{\xi}{2} \begin{bmatrix} -A_\uparrow |d_{yz}\rangle - 2B_\uparrow |d_{x^2-y^2}\rangle \\ A_\uparrow (\sqrt{6} |0\rangle - 2 |2\rangle) + 2B_\uparrow |-1\rangle \end{bmatrix}; \quad (5)$$

As before a nonzero spin-down component will open a new HOMO spin-up-related channel, making two channels available for transport. One can observe however that now

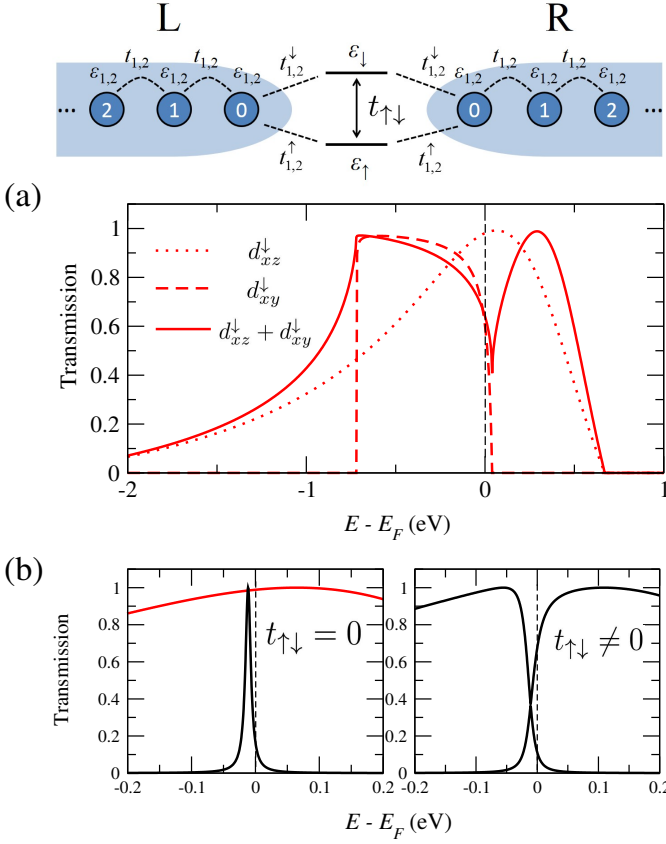


FIG. 4: Minimal tight-binding model explaining DFT results without SOC (a) and with SOC (b). (a) A single (spin-down) level couples to two bands. The rather smooth transmissions due to the d_{xz}^{\downarrow} band (dotted line) develops a pronounced dip right above E_F if the coupling to the d_{xy}^{\downarrow} band is switched on. (b) Transmission eigenvalues mediated by two levels (each coupled to one band) without (left) and with (right) inter-level hopping, showing two independent or mixed channels, respectively.

$\langle \Psi_{\text{HOMO}}^{\downarrow} | H_{\text{SOC}}^z | \Psi_{\text{HOMO}}^{\uparrow} \rangle \neq 0$. For this reason the two channels will be mixed. The conclusions confirm our previous observations in the context of Fig. 3.

Based on the above arguments, we can understand main features of our DFT results by setting up an appropriate tight-binding (TB) model with the following Hamiltonian:

$$\begin{aligned}
 H = & \sum_{\alpha=\uparrow,\downarrow} \alpha \hat{c}_{\alpha}^{\dagger} \hat{c}_{\alpha} + (t_{\uparrow\downarrow} \hat{c}_{\uparrow}^{\dagger} \hat{c}_{\downarrow} + \text{H.c.}) + \\
 & \sum_{i=1}^2 \sum_{j \in L,R} [t_i \hat{c}_{i,j}^{\dagger} \hat{c}_{i,j} + (t_i \hat{c}_{i,j}^{\dagger} \hat{c}_{i,j+1} + \text{H.c.})] + \\
 & \sum_{\alpha=\uparrow,\downarrow} \sum_{i=1}^2 [t_i^{\alpha} \hat{c}_{\alpha}^{\dagger} \hat{c}_{i,L0} + t_i^{\alpha} \hat{c}_{\alpha}^{\dagger} \hat{c}_{i,R0} + \text{H.c.}] :
 \end{aligned} \quad (6)$$

Here the first line considers HOMO spin-up and spin-down levels with the hopping $t_{\uparrow\downarrow}$ between them, the second line describes the left and right semi-infinite Ni chains with two

bands, and the third line refers to the coupling between the molecular levels and the two bands of the chains. We extracted required TB parameters from *ab initio* calculations by inspecting the band structures and by projecting the self-consistent Hamiltonian within the plane-wave basis onto atomic orbitals contained in the pseudo-potential files for each atom type. To double-check and refine our TB parameters, maximally localized Wannier functions were also used to reproduce electronic bands and transmissions of plane-wave DFT calculations. This was accomplished using WANNIER90³⁹ code. A good agreement was found between Wannier TB and our TB Hamiltonian as can be seen in Fig. 5 in the supplementary material.

We first model the transmission dip in the spin-down channel in the absence of SOC. For this purpose we consider two bands, a wide d_{xz}^{\downarrow} band ($\epsilon_1 = -0.93$ eV, $t_1 = 0.8$ eV) and a narrow d_{xy}^{\downarrow} band ($\epsilon_2 = -0.34$ eV, $t_2 = -0.19$ eV), which can couple to the HOMO spin-down orbital at energy $\epsilon_{\downarrow} = -0.25$ eV (it is not seen in Fig. 2a due to strong hybridization with the d_{xz}^{\downarrow} and d_{xy}^{\downarrow}). As seen in Fig. 4(a), when the HOMO couples only to d_{xz}^{\downarrow} ($t_1^{\downarrow} = -0.45$ eV) or to d_{xy}^{\downarrow} ($t_2^{\downarrow} = 0.21$ eV), regular-shaped transmissions without a dip are obtained.

When both couplings are taken into account however, a dip in transmission develops right above the d_{xy}^{\downarrow} band edge at $E - E_F = 0.04$ eV, in agreement with the *ab initio* results in Fig. 2(b). This dip can be seen as a result of destructive quantum interference between two pathways as follows. At energies $E - E_F < 0.04$ eV the d_{xy}^{\downarrow} Ni states form an additional conduction channel in the Ni chain, while for $E - E_F > 0.04$ eV they contribute to an extra density of states (DOS) at the apex Ni atoms due to hybridization with the HOMO orbital. Those states will provide a second pathway for electron propagation: Ni $d_{xz}^{\downarrow} \rightarrow$ HOMO spin-down \rightarrow Ni-apex $d_{xy}^{\downarrow} \rightarrow$ HOMO spin-down \rightarrow Ni d_{xz}^{\downarrow} , in addition to the direct pathway: Ni $d_{xz}^{\downarrow} \rightarrow$ HOMO spin-down \rightarrow Ni d_{xz}^{\downarrow} . Since both pathways involve the same terminal d_{xz}^{\downarrow} Ni band they will interfere (destructively) producing the observed antiresonance in the transmission.

We analyze now the case with SOC, aiming at explaining in particular the sharp transmission feature just below the Fermi energy (see Fig. 2(c)), which is very different for the two magnetic orientations. Both HOMO spin-up and spin-down molecular orbitals need to be included ($\epsilon_{\uparrow} = -0.015$ eV, $\epsilon_{\downarrow} = -0.25$ eV), which couple to two Ni bands, d_{yz}^{\downarrow} (channel 1) and d_{xz}^{\downarrow} (channel 2) ($\epsilon_{1,2} = -0.93$ eV, $t_{1,2} = 0.8$ eV). Two other bands, d_{xy}^{\downarrow} and $d_{x^2-y^2}^{\downarrow}$, are not relevant here and are disregarded for simplicity (or can be considered as admixing in some minor proportion into two main channels mentioned above). The hopping parameters are set to $t_1^{\uparrow} = 0.05$ eV and $t_2^{\downarrow} = -0.45$ eV, where the absolute value of t_1^{\uparrow} is much smaller than those of t_2^{\downarrow} since it is purely due to SOC, while $t_1^{\downarrow} = t_2^{\uparrow} = 0$. In the case of $\mathbf{M} \parallel \mathbf{x}$, as Eq. 4 shows, the two HOMO states are not mixed ($t_{\uparrow\downarrow} = 0$) and couple to the two independent Ni bands, which naturally yields two independent conduction channels, see Fig. 4(b). In the case of $\mathbf{M} \parallel \mathbf{z}$ (see Eq. 5) a small inter-level hopping of $t_{\uparrow\downarrow} = 0.06$ eV should be introduced, which turns out to mix the two channels and

leads to their crossing, see Fig. 4(b). This simple model essentially reproduces our DFT results (Fig. 3). Two key parameters introduced above, t_{\uparrow}^{\dagger} and t_{\downarrow} , originate purely from SOC at the Ni/molecule contacts and depend both on Ni SOC strength and on the HOMO composition (which can be inferred from Eqs.3,4,5). Unlike other parameters (which could be extracted from the DFT Hamiltonian as discussed above), t_{\uparrow}^{\dagger} and t_{\downarrow} were determined by fitting the width (controlled by t_{\uparrow}^{\dagger}) and the shape (controlled by t_{\downarrow}) of model transmissions to DFT curves in Fig. 3.

Finally, it should be emphasized that the tilting of the BDT molecule in the yz plane (see Fig. 2) is crucial for observing both the transmission dip and the M -dependent conduction channel crossing, discussed in Fig. 4. Due to the tilting, the HOMO will also hybridize with Ni d_{xy} states, in addition to d_{xz} . This is essential for providing (i) an additional pathway for electron propagation, which causes the transmission dip, and (ii) mixing of HOMO spin-up and spin-down states for the $M \parallel z$ orientation, which causes the crossing of the two channels. The latter can be clearly seen from Eqs. 3 and 5, since the two HOMO orbitals remain completely decoupled, if the coefficient $B_{\uparrow} = 0$, which is the case for a straight molecular orientation.

In conclusion, using fully relativistic DFT calculations, we find a very high and energy-dependent AMR at the Fermi energy in Ni-BDT-Ni molecular junctions. It stems from the SOC term, which opens a new conduction channel via spin-flip processes at the ferromagnet-molecule interface. In the absence of SOC, the channel was fully blocked due to the symmetry mismatch between the involved HOMO orbital and the Ni electrode states. Importantly, this HOMO-related conductance change is very sensitive to the magnetization direction, resulting in a giant AMR right at the Fermi level. Moreover, a significant AMR of about 95% is found just above E_F due to quantum interference effects. A simple tight-binding model explains the main features of our *ab initio* results. Since the geometry of a molecular junction depends on electrode separation, the AMR can be tuned by mechanical control, as shown in Fig. 6 in the supplementary material. We expect that the proposed mechanism, based on orbital symmetry reasonings, is generally at work in metal-molecule-metal junctions and explains the high AMR values reported recently^{21,23}. Our study reveals the general principles that lead to an enhanced AMR in molecule-based spintronic devices.

Acknowledgments: During this research project, D.L. was supported by the Alexander von Humboldt Foundation through a Fellowship for Postdoctoral Researchers. Furthermore, D.L. and F.P. acknowledge financial support from the Collaborative Research Center (SFB) 767 of the German Research Foundation (DFG). Part of the numerical modeling was performed using the computational resources of the bwHPC program, namely the bwUniCluster and the JUSTUS HPC facility.

Appendix A: Geometry optimization

The geometry optimization of molecular junctions was performed in a supercell containing a single BDT molecule and two four-atom Ni pyramids attached to a Ni(111)- 4×4 periodic slab with 16 atoms per layer and with five and four layers on left and right sides, respectively. During the ionic relaxation the three outermost Ni layers on both sides were kept fixed at bulk structures, while the molecule and the other slab layers were allowed to relax until atomic forces fell below 10^{-3} Ry/Bohr. The geometry optimization was performed using a $2 \times 2 \times 1$ k-point mesh. A plane-wave basis was employed with an energy cutoff of 30 and 300 Ry for wavefunctions and the charge density, respectively.

Appendix B: Transmission calculations of junctions

Ab initio transport properties including SOC were evaluated with the PWCOND code³³. Here the Ni(111) crystalline electrodes were replaced by semi-infinite atomic chains. The SOC effect was taken into account via fully relativistic pseudopotentials³⁴. The Hamiltonian is therefore a 2×2 matrix in spin space, and the non-diagonal matrix elements arise from SOC. All the calculations were done in the non-collinear mode with the specific magnetization direction aligned along z or x axes. Separate calculations were performed for the leads (complex band structure calculations) and scattering regions, which were combined using the wave-function matching technique. The self-consistency criterion in the DFT calculations was set to 10^{-8} Ry in order to obtain well-converged charge and spin magnetization densities.

Our TB parameters, including on-site energies and hopping integrals, were extracted from *ab initio* QE calculations by projecting the self-consistent Hamiltonian onto the basis of atomic wave functions provided by pseudo-potential files. This procedure is rather similar to the one used for calculating the projected density of states (PDOS). Only nearest-neighbor hopping is considered in Ni wires. To calculate couplings of molecular orbitals to Ni electrodes we first diagonalize the molecular Hamiltonian – the Hamiltonian matrix restricted to the molecule atomic orbitals – and then rotates the molecule coupling matrices from the atomic basis to molecular orbitals. We keep then only HOMO orbital and its coupling constants to the contact Ni atoms.

To validate our minimal TB model and adjust TB parameters, we compare it with transmission calculations based on Wannier functions (WFs) which represent also a localized basis set (Fig. S2). The WFs and the Hamiltonian were constructed from DFT Hamiltonian using WANNIER90³⁹ code. Since WFs represent a complete basis set by construction (in an energy window of interest), the total spin down WFs transmission (top panel, dashed line) is in a very good agreement with the DFT curve in Fig. 2(b) of the main text. To compare directly with the TB model, we calculated the transmission only through the HOMO by setting artificially to zero coupling parameters for all other molecular orbitals (top panel, blue line). Finally, this HOMO transmission is further de-

composed into d_{xy} - and d_{xz} -like components by keeping the coupling of HOMO to only d_{xy} or d_{xz} Ni bands, respectively. Comparing two panels of Fig. 5 we can deduce that our minimal TB Hamiltonian (with parameters presented in the main text) gives transmission curves (bottom panel, the same as in Fig. 4(a) of the main text) which agree rather well to “exact”

Wannier-based ones (top panel).

Appendix C: Controlling AMR via a mechanical strain

-
- * Electronic address: donli@dtu.dk
- ¹ M. Bode, S. Heinze, A. Kubetzka, O. Pietzsch, X. Nie, G. Bihlmayer, S. Blügel, and R. Wiesendanger, *Phys. Rev. Lett.* **89**, 237205 (2002).
 - ² K. von Bergmann, M. Menzel, D. Serrate, Y. Yoshida, S. Schröder, P. Ferriani, A. Kubetzka, R. Wiesendanger, and S. Heinze, *Phys. Rev. B* **86**, 134422 (2012).
 - ³ N. Néel, S. Schröder, N. Ruppelt, P. Ferriani, J. Kröger, R. Berndt, and S. Heinze, *Phys. Rev. Lett.* **110**, 037202 (2013).
 - ⁴ J. Schöneberg, P. Ferriani, S. Heinze, A. Weismann, and R. Berndt, *Phys. Rev. B* **97**, 041114(R) (2018).
 - ⁵ C. Gould, C. Rüster, T. Jungwirth, E. Girgis, G. M. Schott, R. Giraud, K. Brunner, G. Schmidt, and L. W. Molenkamp, *Phys. Rev. Lett.* **93**, 117203 (2004).
 - ⁶ C. Rüster, C. Gould, T. Jungwirth, J. Sinova, G. M. Schott, R. Giraud, K. Brunner, G. Schmidt, and L. W. Molenkamp, *Phys. Rev. Lett.* **94**, 027203 (2005).
 - ⁷ A. D. Giddings, M. N. Khalid, T. Jungwirth, J. Wunderlich, S. Yasin, R. P. Campion, K. W. Edmonds, J. Sinova, K. Ito, K.-Y. Wang, et al., *Phys. Rev. Lett.* **94**, 127202 (2005).
 - ⁸ J. D. Burton and E. Y. Tsybal, *Phys. Rev. B* **93**, 024419 (2016).
 - ⁹ J. Velez, R. F. Sabirianov, S. S. Jaswal, and E. Y. Tsybal, *Phys. Rev. Lett.* **94**, 127203 (2005).
 - ¹⁰ D. Jacob, J. Fernández-Rossier, and J. J. Palacios, *Phys. Rev. B* **77**, 165412 (2008).
 - ¹¹ G. Autès, C. Barreateau, D. Spanjaard, and M. C. Desjonquères, *Phys. Rev. B* **77**, 155437 (2008).
 - ¹² V. M. García-Suárez, D. Z. Manrique, C. J. Lambert, and J. Ferrer, *Phys. Rev. B* **79**, 060408(R) (2009).
 - ¹³ M. Häfner, J. K. Viljas, and J. C. Cuevas, *Phys. Rev. B* **79**, 140410(R) (2009).
 - ¹⁴ M. Viret, M. Gabureac, F. Ott, C. Fermon, C. Barreateau, G. Autes, and R. Guirado-Lopez, *Eur. Phys. J. B* **51**, 1 (2006).
 - ¹⁵ A. Sokolov, C. Zhang, E. Y. Tsybal, J. Redepenning, and B. Doudin, *Nat. Nanotechnol.* **2**, 171 (2007).
 - ¹⁶ S. Egle, C. Bacca, H.-F. Pernau, M. Huefner, D. Hinzke, U. Nowak, and E. Scheer, *Phys. Rev. B* **81**, 134402 (2010).
 - ¹⁷ J. Schöneberg, F. Otte, N. Nel, A. Weismann, Y. Mokrousov, J. Krger, R. Berndt, and S. Heinze, *Nano Lett.* **16**, 1450 (2016).
 - ¹⁸ J. Wunderlich, T. Jungwirth, B. Kaestner, A. C. Irvine, A. B. Shick, N. Stone, K.-Y. Wang, U. Rana, A. D. Giddings, C. T. Foxon, et al., *Phys. Rev. Lett.* **97**, 077201 (2006).
 - ¹⁹ R. Yamada, M. Noguchi, and H. Tada, *App. Phys. Lett.* **98**, 053110 (2011).
 - ²⁰ M. Grünewald, M. Wahler, F. Schumann, M. Michelfeit, C. Gould, R. Schmidt, F. Würthner, G. Schmidt, and L. W. Molenkamp, *Phys. Rev. B* **84**, 125208 (2011).
 - ²¹ J. J. Li et al., *J. Am. Chem. Soc.* **137**, 5923 (2015).
 - ²² D. Rakhmilevitch, S. Sarkar, O. Bitton, L. Kronik, and O. Tal, *Nano Lett.* **16**, 1741 (2016).
 - ²³ K. Yang et al., *Nat. Commun.* **10**, 1 (2019).
 - ²⁴ F. Otte, S. Heinze, and Y. Mokrousov, *Phys. Rev. B* **92**, 220411(R) (2015).
 - ²⁵ T. McGuire and R. L. Potter, *IEEE Trans. Magn.* **11**, 1018 (1975).
 - ²⁶ P. Gambardella, A. Dallmeyer, K. Maiti, M. C. Malagoli, W. Eberhardt, K. Kern, and C. Carbone, *Nature* **416**, 301 (2002).
 - ²⁷ A. Smogunov and Y. J. Dappe, *Nano Lett.* **15**, 3552 (2015).
 - ²⁸ D. Li, *Phys. Rev. B* **99**, 174438 (2019).
 - ²⁹ D. Li, R. Banerjee, S. Mondal, I. Maliyov, M. Romanova, Y. J. Dappe, and A. Smogunov, *Phys. Rev. B* **99**, 115403 (2019).
 - ³⁰ A. N. Pal, D. Li, S. Sarkar, S. Chakrabarti, A. Vilan, L. Kronik, A. Smogunov, and O. Tal, *Nature communications* **10**, 1 (2019).
 - ³¹ V. V. Maslyuk, A. Bagrets, V. Meded, A. Arnold, F. Evers, M. Brandbyge, T. Bredow, and I. Mertig, *Phys. Rev. Lett.* **97**, 097201 (2006).
 - ³² P. Giannozzi et al., *J. Phys. Condens. Matter* **21**, 395502 (2009).
 - ³³ A. Smogunov, A. Dal Corso, and E. Tosatti, *Phys. Rev. B* **70**, 045417 (2004).
 - ³⁴ A. Dal Corso, A. Smogunov, and E. Tosatti, *Phys. Rev. B* **74**, 045429 (2006).
 - ³⁵ D. A. Ryndyk, A. Donarini, M. Grifoni, and K. Richter, *Phys. Rev. B* **88**, 085404 (2013).
 - ³⁶ M. A. Karimi, S. G. Bahoosh, M. Herz, R. Hayakawa, F. Pauly, and E. Scheer, *Nano Lett.* **16**, 1803 (2016).
 - ³⁷ D. Li, Y. J. Dappe, and A. Smogunov, *J. Phys. Condens. Matter* **31**, 405301 (2019).
 - ³⁸ M. Strange, C. Rostgaard, H. Häkkinen, and K. S. Thygesen, *Phys. Rev. B* **83**, 115108 (2011).
 - ³⁹ A. A. Mostofi, J. R. Yates, Y.-S. Lee, I. Souza, D. Vanderbilt, and N. Marzari, *Comput. Phys. Commun* **178**, 685 (2008).

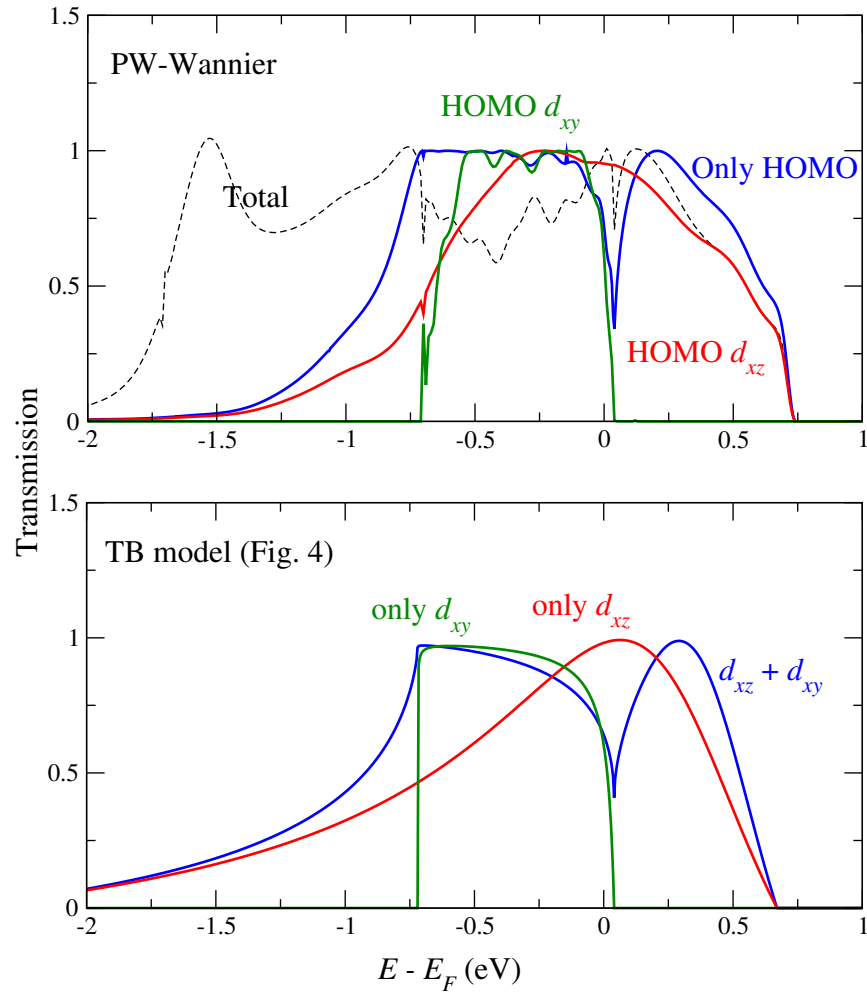


FIG. 5: Comparison of transmission functions calculated with Wannier functions Hamiltonian (top) and with the minimal TB model presented in the main text (bottom).

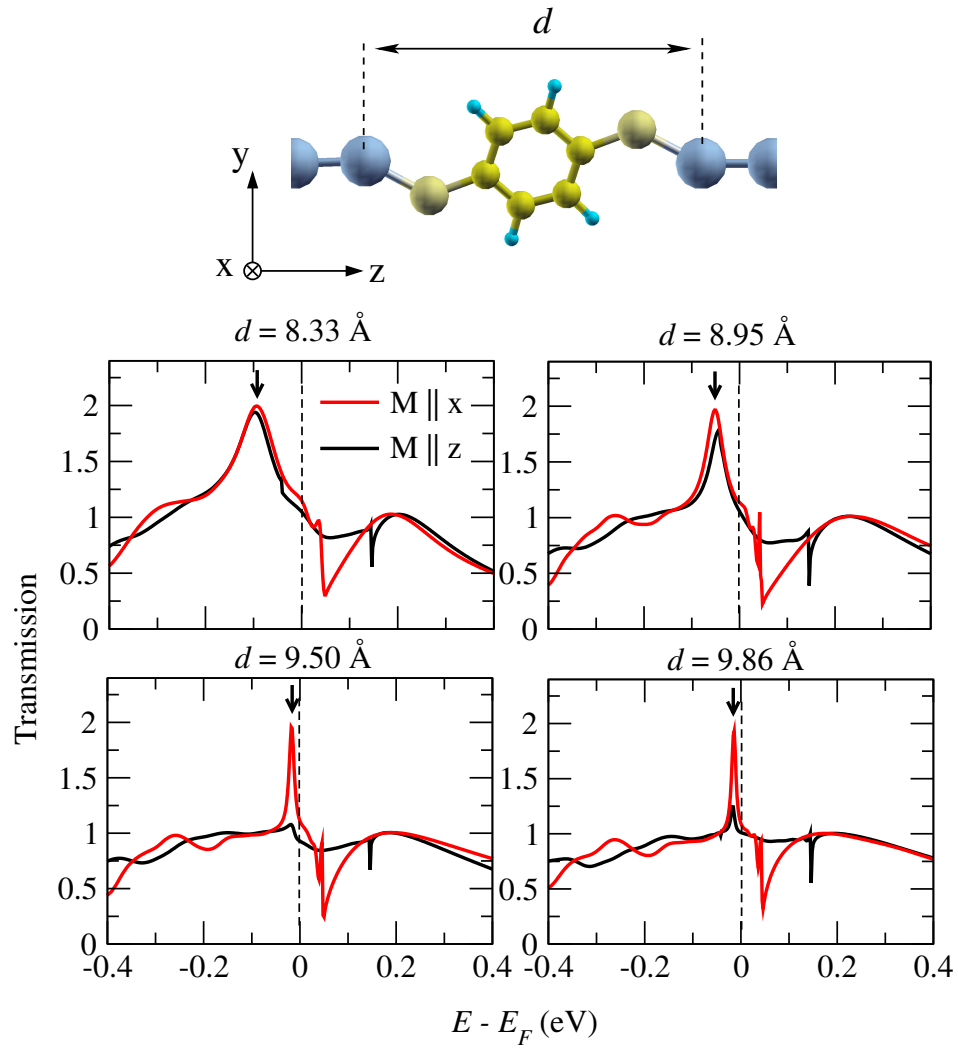


FIG. 6: Controlling AMR via electrode separation. The degree of MAMR just below E_F (marked with a downward-pointing arrow) can be tuned by stretching of the molecular junction due to a competition between hybridization and SOC effects.